We are IntechOpen,
the world's leading publisher of
Open Access books
Built by scientists, for scientists

6,900
Open access books available

186,000
International authors and editors

200M
Downloads

154
Countries delivered to

Our authors are among the

TOP 1%
most cited scientists

12.2%
Contributors from top 500 universities

CLARIVATE ANALYTICS

BOOK CITATION INDEX

INDEXED

WEB OF SCIENCE™

Selection of our books indexed in the Book Citation Index
in Web of Science™ Core Collection (BKCI)

Interested in publishing with us?
Contact book.department@intechopen.com

Numbers displayed above are based on latest data collected.
For more information visit www.intechopen.com

Using Raman Spectroscopy to Improve Hyperpolarized Noble Gas Production for Clinical Lung Imaging Techniques

Jonathan Birchall, Nicholas Whiting, Jason Skinner,

Michael J. Barlow and Boyd M. Goodson

Additional information is available at the end of the chapter

Abstract

Spin-exchange optical pumping (SEOP) can be used to "hyperpolarize" ^{129}Xe for human lung MRI. SEOP involves transfer of angular momentum from light to an alkali metal (Rb) vapor, and then onto ^{129}Xe nuclear spins during collisions; collisions between excited Rb and N_2 ensure that incident optical energy is nonradiatively converted into heat. However, because variables that govern SEOP are temperature-dependent, the excess heat can complicate efforts to maximize spin polarization—particularly at high laser fluxes and xenon densities. Ultra-low frequency Raman spectroscopy may be used to perform *in situ* gas temperature measurements to investigate the interplay of energy thermalization and SEOP dynamics. Experimental configurations include an "orthogonal" pump-and-probe design and a newer "inline" design (with source and detector on the same axis) that has provided a >20-fold improvement in SNR. The relationship between ^{129}Xe polarization and the spatiotemporal distribution of N_2 rotational temperatures has been investigated as a function of incident laser flux, exterior cell temperature, and gas composition. Significantly elevated gas temperatures have been observed —hundreds of degrees hotter than exterior cell surfaces—and variances with position and time can indicate underlying energy transport, convection, and Rb mass-transport processes that, if not controlled, can negatively impact ^{129}Xe hyperpolarization.

Keywords: low-frequency Raman, hyperpolarization, spin-exchange optical pumping, xenon NMR/MRI, low-field NMR, remote temperature measurement

1. Introduction

Magnetic resonance imaging (MRI) is a powerful tool for diagnostic imaging of soft tissue, combining superior contrast, dynamic capability, and no risk of damage caused by ionizing radiation compared to computerized tomography (CT) [1]. Most MRI techniques conveniently detect the nuclear spin of protons in water, which makes up a significant portion of the human body. This detection modality poses a problem within the lungs, however, as the low proton density translates to greatly reduced signal-to-noise ratios for conventional MRI techniques. Even at high magnetic field strengths, the equilibrium nuclear spin polarization is very low (~10^{-4} to 10^{-6}). To facilitate MRI inside the lungs, far greater signal-to-noise ratios are needed, requiring nuclear spin polarizations to be increased far above equilibrium levels—a process known as hyperpolarization. Indeed, inhalation of hyperpolarized gases provides greatly improved sensitivity and bright images, outweighing the low spin densities of the gas phase. Gas hyperpolarization can now be readily achieved using established techniques; however in these approaches, maximizing the available spin polarization is hampered by complex system dynamics and codependence of many variables that are heavily temperature-dependent.

In most studies relevant to lung imaging, this hyperpolarized state is achieved by utilizing circularly polarized photons to shift particles with a nonzero magnetic moment between discrete spin states. During gas-phase collisions, spin angular momentum is transferred from alkali metal electrons to noble gas nuclei, a technique known as spin-exchange optical pumping (SEOP) [2]. Noble gases are used in SEOP because of their lack of reactivity with alkali metal vapors and their ultra-long hyperpolarization lifetimes. Nitrogen is present as a buffer gas to prevent radiation trapping, helping to maximize the alkali metal electron spin polarization—and hence, the noble gas nuclear spin polarization. Thus, inhalation of a hyperpolarized noble gas sample such as ^{129}Xe while inside the MRI scanner enables both structural and functional high-resolution imaging of the lungs in real time. Despite significant advances in polarizer technology in recent years, many underlying aspects of the SEOP process, such as energy- and mass transport mechanisms within the OP cell and the temperature dependences of many parameters, remain poorly understood. Ironically, the desire to maximize the available nuclear spin magnetization leads to a demand for higher pump laser powers and richer noble gas mixtures, which only serve to compound this issue.

In an attempt to overcome these challenges, Raman spectroscopy may be used to complement more commonly used techniques such as optical absorption spectroscopy and low-field NMR in order to optimize the multidimensional SEOP parameter space, thereby improving the ^{129}Xe hyperpolarization process for MR applications. Conventional temperature measurement (e.g., using a thermocouple) would be challenging to implement, given that the SEOP process takes place inside a sealed vessel, within a magnetic field, and under constant uniform illumination by high-power laser light; moreover, temperature measurement of the exterior cell walls may often provide only a poor reflection of the true gas behavior within the cell. However, if optical access is available, Raman spectroscopy can be used to acquire *in situ* rotational and vibrational temperature measurements of the nitrogen buffer gas—and hence, an accurate picture of the true gas temperature at a given location within the cell. This capability should provide a more complete

insight into the energy deposition, transport, and dissipation processes that occur during the SEOP process, which in turn may further enable optimization of the efficiency of noble gas hyperpolarization—thereby improving the diagnostic capability of HP noble gases in clinical settings.

2. Theory

2.1. Spin-exchange optical pumping

The SEOP process consists of two major steps. Firstly, circularly polarized photons (necessary to satisfy the selection rules for optical absorption) are used to transfer angular momentum to a gaseous target with nonzero spin, such as spin-½ electrons. A vaporized alkali metal such as rubidium is typically used, since its single outer shell electron is easier to manipulate and existing laser technology at the required transition wavelengths is well developed. The net polarization, P, of the alkali metal can then be given by [3]

$$P = S_z \frac{R}{\Gamma_{SD} + R} \tag{1}$$

where S_z is the photon spin of the circularly polarized laser light, R is the optical pumping rate, and Γ_{SD} is the rate of spin destruction or spin relaxation due to collisions with the walls of the system or other gas-phase species (particularly xenon atoms). Assuming the optical pumping rate exceeds the rate of relaxation, a large population excess will accumulate in one of the two electronic spin states, leading to the alkali metal as a whole becoming highly polarized. The particular favored state depends on the directional helicity of the light.

The second stage in the SEOP process is that of spin-exchange. Bringing an unpolarized gaseous system into contact with the polarized alkali metal vapor results in spin-coupling via a hyperfine interaction. Gas phase collisions then lead to transfer of polarization from alkali metal electrons to noble gas nuclei on short timescales. The net spin polarization of the noble gas during the spin-exchange process is calculated using [3]

$$P_G = P_A \frac{\Gamma_{SE}}{\Gamma_{SE} + \Gamma_{SD}} \left[1 - e^{-t(\Gamma_{SE} + \Gamma_{SD})} \right] \tag{2}$$

where P_G and P_A represent the net spin polarizations of the gas and alkali metal, respectively, Γ_{SE} is the rate of spin exchange between alkali metal electrons and gas nuclei, Γ_{SD} is the rate of alkali metal electron spin destruction, and t is the time elapsed after the commencement of laser polarization in seconds. The SEOP process requires temperatures on the order of 100°C to ensure sufficient alkali metal vapor density. Buffer gases such as nitrogen is commonly used to quench radiation trapping and slow the rate of electron spin relaxation to help maintain high net spin polarizations by preventing unwanted fluorescence and re-absorption of unpolarized light [4] by alkali metal electrons. An overview of the SEOP process is illustrated in **Figure 1**.
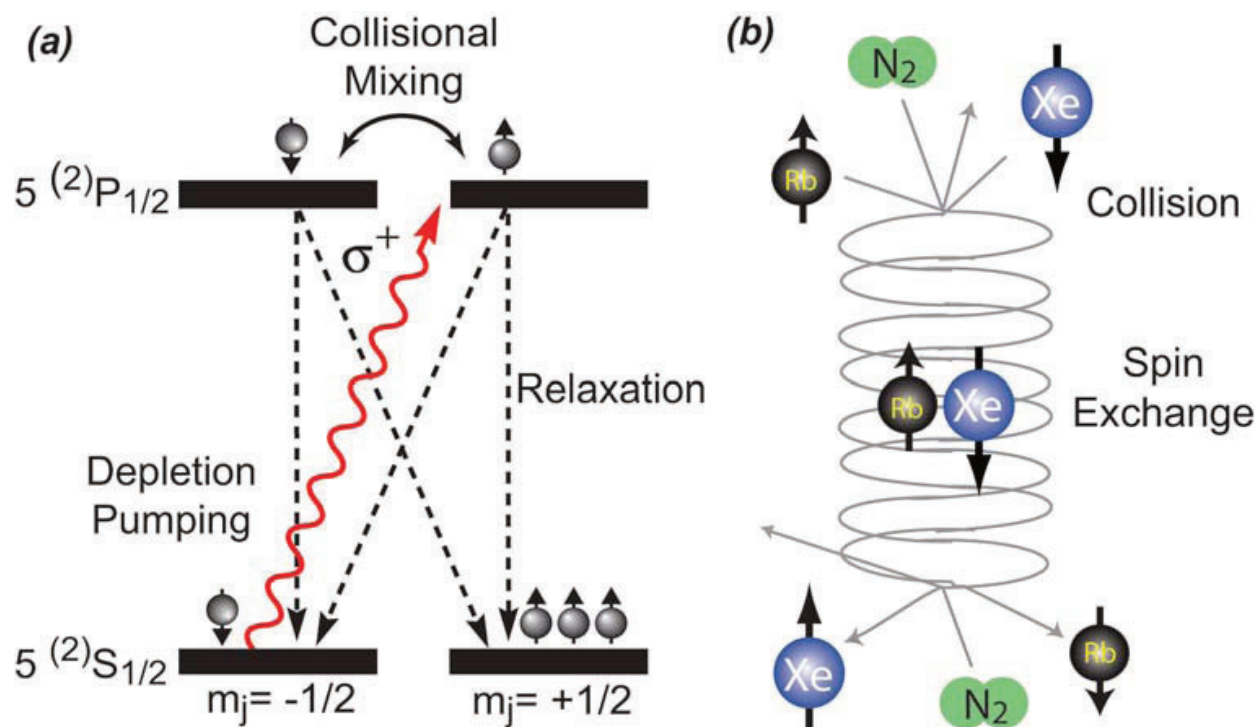
Figure 1. The spin-exchange optical pumping (SEOP) process. (a) Optical pumping and collisional mixing of the alkali metal electron spin states using circularly polarized light. (b) Polarization of noble gas nuclei via collision and spin-exchange process in the formation and breakup of an alkali-metal/noble-gas van der Waals molecule. Figures adapted from [7].

As previously mentioned, temperature is one of the most important variables governing the SEOP process. Elevated temperatures raise the alkali metal vapor density within the cell, increasing the probability of collisions between pump laser photons and alkali metal electrons and more importantly resulting in increased spin-exchange rates. As evidenced by Eq. (2), the latter effect should lead to a greater net spin polarization of the noble gas, provided there is sufficient pump light intensity to maintain good illumination of the optical cell (and hence, good alkali metal polarization). This prediction holds to a certain extent—as temperature continues to rise however, the alkali metal number density can increase rapidly in a self-propagating fashion; the alkali metal vapor absorbs more light, whose energy is rapidly converted to heat, which can in turn lead to even more alkali metal vaporization. This results in the form of optical opacity, whereby pump laser light is unable to penetrate the length of the optical cell. This actually reduces the efficiency of optical pumping in the areas of the cell furthest from the pump laser, because although the spin-exchange rate may be quite high, the alkali metal polarization in much of the cell is low, greatly reducing noble gas polarization. This is known as a "runaway" process [5, 6], and is clearly detrimental to a stable, efficient SEOP process. In the interest of obtaining the highest possible NMR signal, it is desirable to conduct experiments at an optimal temperature where net spin polarization and build-up rates are maximized, while avoiding the unstable runaway regime.

2.2. Temperature measurement using Raman spectroscopy

As mentioned above, the presence of nitrogen gas inside the optical cell is primarily meant to quench the rate of radiative spin-destruction, achieved by collisions with electronically excited

alkali metal atoms. The energy transferred as a result of these collisions is pooled in the rotational and vibrational modes of the N_2 molecules; these modes quickly relax to the translational degrees of freedom, thereby increasing the local gas temperature inside of the cell. Since SEOP must take place inside a closed system due to the high reactivity of alkali metals in air, physical insertion of a thermocouple is impractical for the reasons listed above, and merely measuring the cell surface temperature does not provide a true account of the internal temperature, nor the corresponding energy transport processes occurring within the cell. Additionally, progressively stronger light sources have been utilized for SEOP over the years, and lasers emitting tens or hundreds of watts of energy are now standard [6]. Virtually all of the laser energy absorbed by Rb is transferred to the rotational and vibrational degrees of freedom in the N_2 buffer gas, which then rapidly equilibrates with the translational temperature (corresponding to the local temperature of the gas mixture). These changes in temperature are capable of significantly affecting SEOP (hence, xenon polarization) through changes to the alkali metal density and absorption profile [8], degradation of organic coatings on the OP cell surface [9], and convective gas transport that may bring xenon in closer proximity to paramagnetic relaxation centers in the cell wall surface [4, 10, 11]; changes to temperature-dependent cross-sections that govern polarization and depolarization rates in SEOP may also occur. Remote sensing of the N_2 rotational (and vibrational) temperatures inside the pump cell during SEOP can be achieved using *in situ* Raman spectroscopy.

Hickman et al. [12] demonstrated that the intensity of each peak, numbered J, in the N_2 Raman spectrum follows the relation

$$I(J) \propto v^4 g(J)(2J+1) P_{J \to J'} e^{-\frac{BJ(J+1)}{k_B T}} \tag{3}$$

where v is the frequency of the rotational line in Hertz, $g(J)$ is the ground state degeneracy due to the nuclear spin, B is the rotational constant for nitrogen (taken to be ~2), k_B is Boltzmann's constant, J is the peak number, and

$$P_{J \to J'} = \frac{3(J+1)(J+2)}{2(2J-1)(2J+1)} \tag{4}$$

Combining Eqns. (3) and (4) produces the relation

$$-BJ(J+1)\frac{hc}{k_B T} = ln\frac{S(J)}{g(J)f(J)} + 4ln\frac{1}{v} \tag{5}$$

where $S(J)$ is the measured intensity of the Raman peak, h is the Planck constant, c is the speed of light in m s^{-1}, and

$$f(J) = \frac{3(J+1)(J+2)}{2(2J+3)} \tag{6}$$

A plot of $F(J) = ln\left[\frac{S(J)}{g(J)f(J)}\right]$ against $J(J+1)$ then yields a straight line with gradient $m = \frac{Bhc}{k_B T}$. Rearranging this equation for T thus allows calculation of the rotational temperature of N_2.

2.3. Hyperpolarized lung imaging

Any noble gas isotope with nonzero spin can theoretically be used as a hyperpolarized contrast agent with a view for clinical lung MRI. Traditionally, helium-3 was most commonly used due to its high gyromagnetic ratio—resulting in stronger MRI signals. However, due to its insolubility in blood and water, perfusion across the alveolar wall cannot occur, primarily limiting the use of [3]He to gas-phase ventilation and diffusion imaging. The difficulty in wide-spread clinical [3]He adoption is further compounded by the difficulty and expense of acquisition, since [3]He is a nonrenewable by-product of tritium decay in nuclear reactors. As such, most current clinical studies on hyperpolarized noble gases use [129]Xe for its solubility in tissue and blood, significant chemical shift range, low cost of acquisition, and high natural abundance.

As discussed previously, higher net spin polarizations directly result in stronger MR signal generation and hence, improved image contrast between areas of interest and background noise. Recent hyperpolarization methods can create near-unity net spin polarizations [13], resulting in spectroscopic signals four to five orders of magnitude greater than nonhyperpolarized samples. Such improvements in image quality facilitate the use of HP noble gas MRI within the lungs as a diagnostic imaging tool for characterizing lung structure and function [14], and consequently may potentially enable earlier and more reliable diagnosis of various respiratory disorders, such as idiopathic pulmonary fibrosis (IPF) and chronic obstructive pulmonary disease (COPD) 7]. An example of a HP [129]Xe lung ventilation image can be seen in **Figure 2**.
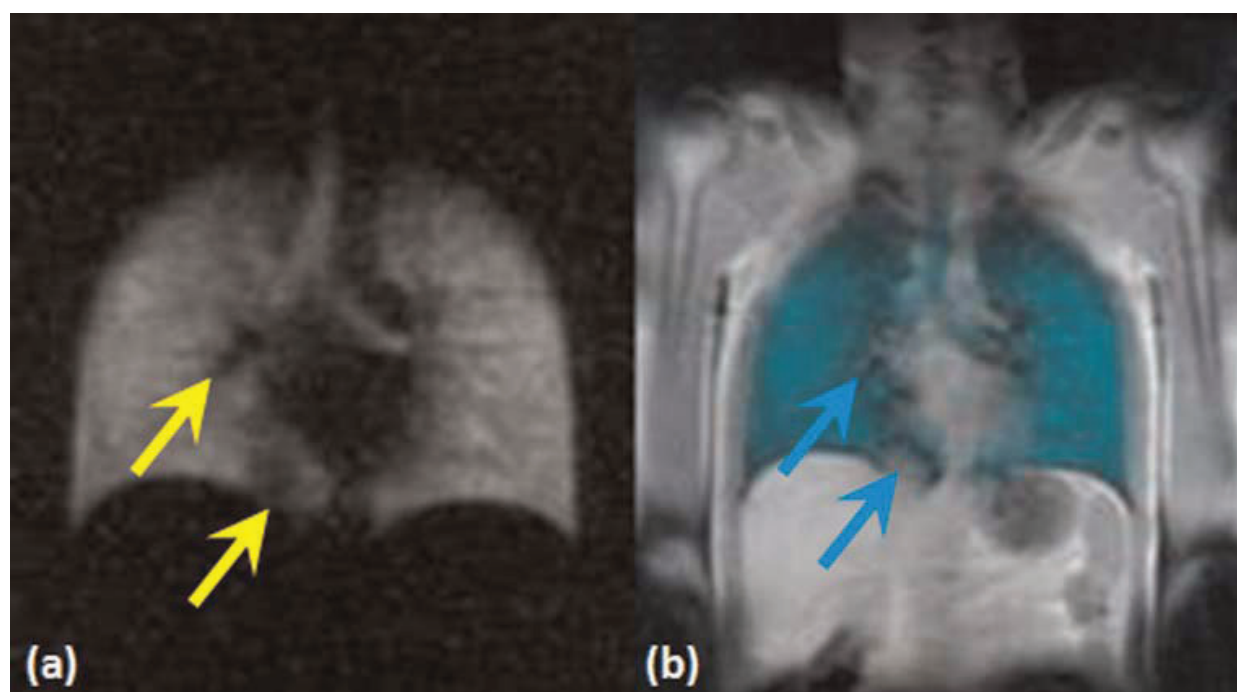

Figure 2. (a) Coronal plane 25 mm slice [129]Xe-MR ventilation image of a healthy adult male, with [129]Xe appearing bright, upper airways are clearly delineated. (b) Second coronal plane 25 mm slice fused [129]Xe-MR ventilation and proton coregistration image, with [129]Xe appearing green blue-green. On the fused image, it can be seen that ventilation defects on the ventilation image (yellow arrows) correspond to a diaphragmatic eventration and pulmonary vasculature on the fused image (blue arrows) [15].

3. Methodology

Early studies carried out by Happer and coworkers [4] used the N_2 rotational temperature to monitor energy transport during optical pumping. These experiments primarily used pump cells loaded with helium and nitrogen gases, and operated under the same experimental conditions as SEOP (without the NMR-active noble gas) using a broadband (2 nm linewidth) 795 nm Rb D_1 pump laser. The Raman setup shown in **Figure 3(a)** consisted of a 514.5 nm probe beam from an argon-ion laser (6 W) that could be focused to a 1 mm waist anywhere within the pump cell; the scattered light was collected using a planoconvex lens and directed into a Spex 1404 double Raman spectrometer (0.85 m focal length) and the photons were counted using a bi-alkali photomultiplier tube (PMT) with computer readout. The results of this work include the observation of convective heat transfer during optical pumping, as the N_2 rotational temperature deviated from a linear relationship with absorbed pump laser power, shown in **Figure 3(b)**. This convective heat transfer was further studied by measuring the N_2 temperature at differing spatial locations throughout the pump cell as a function of pump laser absorption. For low values of laser absorption (2.9 W), the calculated Rayleigh number (which provides a measure of convective vs. conductive transfer by comparing buoyant and viscous forces) indicates conductive heat transfer to the pump cell walls. As the absorption of the pump laser is increased to 15 W, the Rayleigh number indicates convective heat transfer; this is important in SEOP, as convection can affect the residing time of polarized ^{129}Xe nuclei near the pump cell walls and lead to depolarization. Switching between a cell loading of predominantly helium gas with some nitrogen (1.0 and 0.33 amagat) to a cell with only high density nitrogen (3.2 amagat) increased the Rayleigh number by a factor of 70; simply changing the pump cell volume and geometry further increased the Rayleigh number by an additional factor of 29. This demonstrates how gas composition, density, and pump cell geometry can affect energy transport during SEOP.
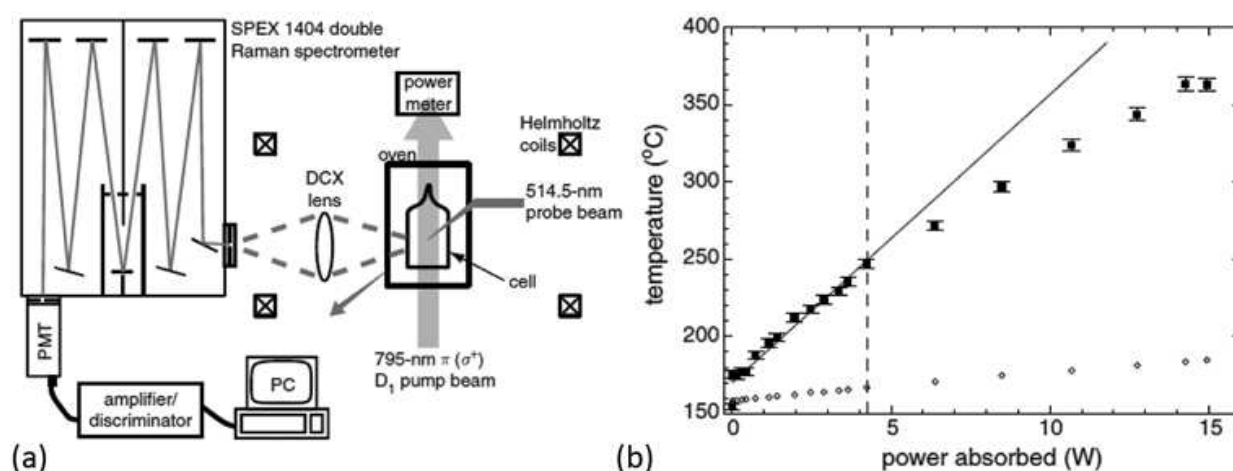

Figure 3. (a) Schematic representation of Happer's experimental setup showing SEOP pump cell, 795 nm Rb excitation source, and orthogonal Raman probe/detect configuration. 514.5 nm Raman probe beam furnished by a 15 W water cooled argon-ion laser, with resulting Raman scattering imaged directly into spectrometer. (b) N_2 rotational temperature (solid squares) as a function of absorbed laser power for a cell loading of 2 amg He and 0.33 amg N_2 in a 40 cm^3 OP cell, with an external cell surface temperature of 170°C (open diamonds). Solid line fits to data points up to 4.3 W of absorbed energy, after which the experimental data deviate significantly from a purely conductive energy dissipation model [2].

Happer et al. also noticed that the N_2 rotational temperature was elevated compared to the surface temperature of the glass walls of the pump cell (measured via thermocouple). The extent of the temperature elevation changed with absorbed pump laser power and gas loading (density/composition), and often varied from 100 to 200°C above the cell wall temperature. Because of the slower vibrational-to-rotational cross-relaxation, N_2 vibrational temperatures were found to be significantly elevated in pump cells containing only nitrogen (T_{vib} ~ 900°C). Upon the addition of helium gas, N_2 vibration temperatures were only elevated ~120°C above the cell surface temperature, due to the significantly faster relaxation time with the helium translational temperature. These studies, which were the first to use Raman spectroscopy to remotely monitor gas temperatures during SEOP, utilized relatively low resonant laser powers and predominantly helium-rich gas loadings—both of which lessen the degree to which energy accumulates in the N_2 rotational-vibrational manifold. The authors noted that additional studies would be warranted under conditions of high resonant laser power and the absence of helium buffer gas.

3.1. Orthogonal configuration

Recent advances in laser diode array (LDA) technology have resulted in not only an increase in overall laser power (hundreds of watts), but also a narrowing of the spectral output from several nanometers to a few tenths of a nanometer. This increase in resonant flux leads to more efficient absorption by the relatively narrow alkali metal D_1 absorption line (c.a. ~0.1 nm), with the consequence of additional thermal management concerns [6]. Furthermore, recent advances in using high xenon partial pressures (p_{Xe}) in SEOP in the absence of helium to attain high xenon nuclear spin polarization values (p_{Xe}) [16], and its further application in clinical-scale xenon hyperpolarizers used for pulmonary imaging [6], have furthered the interest in binary Xe/N_2 gas mixtures for SEOP. The absence of helium, with its favorable thermal conductivity, is expected to further exacerbate thermal management concerns. Because of these demands of high resonant laser flux and gas density/composition, additional studies of energy transport under these conditions is warranted.

Further work from Whiting et al. [17] conducted remote temperature sensing using Raman scattering to observe energy thermalization during $Rb/^{129}Xe$ SEOP under conditions of high xenon partial pressures and resonant laser powers. These studies used a laser diode array (~70 W) that was frequency-narrowed (~0.25 nm linewidth) using an internal volume holographic grating; this SEOP pump laser was spectrally tunable independent of output power to allow comparative studies at different excitation frequencies. The cylindrical optical pumping cell (2.5 cm inner diameter; 15.5 cm length) was surrounded by an outer glass cylinder that served as a forced-air oven and allowed 360° optical access [18]. Miniature NMR coils were placed directly under the OP cell to allow correlative low-field NMR studies of HP ^{129}Xe gas along with Raman scattering measurements of nitrogen buffer gas. The Raman apparatus shown in **Figure 4**(**a**, **c**) consisted of a Verdi V5 532 nm excitation laser (5 W) that was fiber-coupled to a modular lens assembly box to focus the light into the OP cell. Scattered light was collected by a similar lens box (positioned orthogonal to the probe laser) that was fiber-coupled to a Horiba Jobin-Yvon U1000 double 1-m Raman spectrometer with 2400 l/mm grating and CCD receiver. Spatial filtering of the laser and Rayleigh scatter was achieved through

adjustment of the internal baffles of the spectrometer; this provided spectra that displayed Stokes and anti-Stokes rotational Raman lines within 6 cm^{-1} of the laser line without the use of notch or edge filters—see **Figure 4(b)**. The N_2 rotational temperature was calculated using the methods explained in Section 2.2, and calibration studies showed a good correlation with different N_2 gas temperatures in the absence of optical pumping as shown in **Figure 4(d)**.
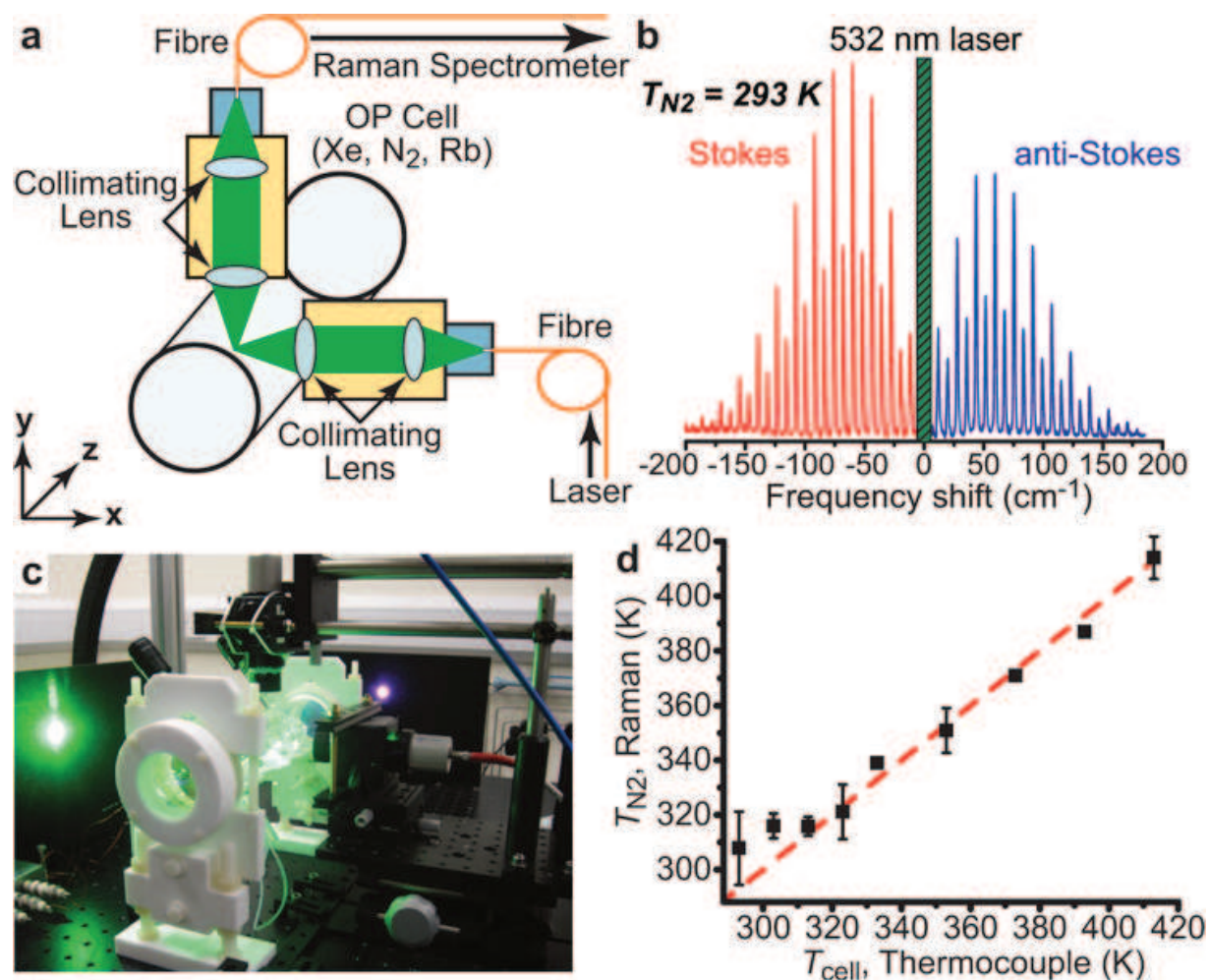

Figure 4. (a) Schematic representation of orthogonal Raman apparatus. (b) Example N_2 rotational Raman spectrum (baseline-corrected) at room temperature, without SEOP (3 atm N_2). (c) Photograph of orthogonal Raman apparatus. (d) Plot of oven temperature (T_{cell}) measured via thermocouple (located in the oven inlet airstream) versus T_{N2} measured via Raman spectroscopy without SEOP; experimental data (squares) are shown in comparison with simulation assuming 1:1 correlation (dotted line); error bars are least-squares fit errors of Bhc/kT plots [19].

In this work, different xenon partial pressures were studied to determine the effects from increasing incident laser power on both ^{129}Xe hyperpolarization level and N_2 rotational temperature—see **Figure 5(a, b)**. Both HP ^{129}Xe signal and N_2 rotational temperatures increased with laser power for the different gas loadings (100/1900, 500/1500, and 1500/500 Torr Xe/N_2), with the highest ^{129}Xe signal and N_2 temperature observed at the highest xenon partial pressure. This increased temperature at high xenon partial pressure was not primarily attributed to increased laser absorption, but rather to the combination of the lower concentration of nitrogen (increasing the energy absorption per N_2) and low thermal conductivity of xenon

(which was the significant fraction of total gas volume). Gas loadings with the lowest xenon partial pressure exhibited a relatively weak dependence of N_2 rotational temperature on incident laser light. Despite the high nitrogen temperatures, the high xenon density loading provided the highest overall [129]Xe NMR signal—typically the overall figure of merit for applications of hyperpolarized contrast agents.

Additional studies examined the effects of heating as a function of longitudinal position within the cylindrical pump cell. Because the external heat source was provided in the rear of the cell, and the forced air oven was poorly insulated, there was a significant temperature gradient (~30–40°C surface temperature) along the length of the cell. Both the [129]Xe NMR signal and the N_2 rotational temperature reflected the presence of this gradient and showed the maximal values were at the rear of the cell (close to the heating source). This type of back-to-front temperature gradient has both benefits and detriments. One benefit is that the total cell illumination may improve, as the optical density of absorbers gradually increases with pene-tration depth (unlike other OP systems, which may have conditions where all the laser light is absorbed in the front portion of the cell—leaving the rear of the cell optically opaque); this improved illumination should increase global HP [129]Xe signal. On the other hand, an unfavor-able result of temperature gradients is longitudinal convective heat transport, which poten-tially brings the polarized gas in close contact with paramagnetic relaxation centers in the cell wall surface for longer periods of time. These studies were carried out at different illumination wavelengths to examine how changes to the Rb D1 lineshape [6] (through altering the gas density and composition) affect the N_2 rotational temperature. The highest HP [129]Xe NMR signals and N_2 rotational temperatures were found nearest to the Rb D_1 line, and elevated values were observed at red-shifted excitation wavelengths (as expected, given the effects of different gas loadings on the Rb absorption lineshape [6]).

The effects of slight changes in temperature of the forced air oven on both HP [129]Xe NMR signal and N_2 rotational temperature over the course of an SEOP experiment were also moni-tored—see **Figure 5(c, d)**. Increasing the external cell temperature from ~110°C to ~140°C resulted in significant changes to these parameters. At the lower cell temperature, the N_2 rotational temperature reached steady state (~190°C) quickly and held the value throughout the course of the experiment (40 min); correspondingly, other conditions within the OP cell remained stable (e.g., laser absorption, Rb density, P_{Xe} value, etc.). By raising the external cell temperature a mere ~30°C, the N_2 rotational temperature climbed to ~730°C in less than 15 minutes of OP; a steep rise in HP [129]Xe signal was also observed in the initial portion of the SEOP experiment. However, once the N_2 rotational temperature peaks, both it and the P_{Xe} values begin to drop significantly. The N_2 rotational temperature remains quite high (~530°C), but fluctuates greatly over the remainder of the experiment; the amount of absorbed laser light continues to increase for the remainder of the experiment. These occurrences likely indicate both Rb runaway as well as increased turbulence inside the OP cell. These results, showing the effects of slight external cell surface temperature changes on the SEOP efficiency, indicate that (under some experimental regimes) overall cell illumination can be more critical than the Rb/[129]Xe spin-exchange rate (which is often viewed as the most important parameter of SEOP).

In summary, this work expanded on the previous studies of Happer et al. [4] by examining a regime of high resonant laser power and xenon-dominant binary gas mixtures in the absence of

helium. It also used *in situ* low-field ^{129}Xe NMR in addition to the N_2 rotational temperatures observed using Raman spectroscopy. These relatively extreme conditions showed that elevated N_2 rotational temperatures correlated with ^{129}Xe hyperpolarization across a range of experimental conditions and that internal gas temperatures of ~730°C could be observed within 15 minutes of SEOP. While the results of these experiments effectively displayed the interdependence of laser power, cell temperature, gas density/composition, and laser centroid offset during SEOP, the experimental Raman setup could be significantly improved. Although the internal baffles of the Raman spectrometer were used for spectral/spatial filtering (in the absence of notch or edge filters), detection sensitivity was an issue, as were significant problems with the baseline. Furthermore, the orthogonal excitation/detection setup was difficult to precisely focus (with an associated hysteresis). Both the probe beam and Raman scattering collection optics needed to be focused to the same point within ~1 mm spatial resolution in three dimensions using only manual translational stages. An improved design, in which the excitation and collection optics were colinear, would simplify the setup and overcome many of these shortfalls.
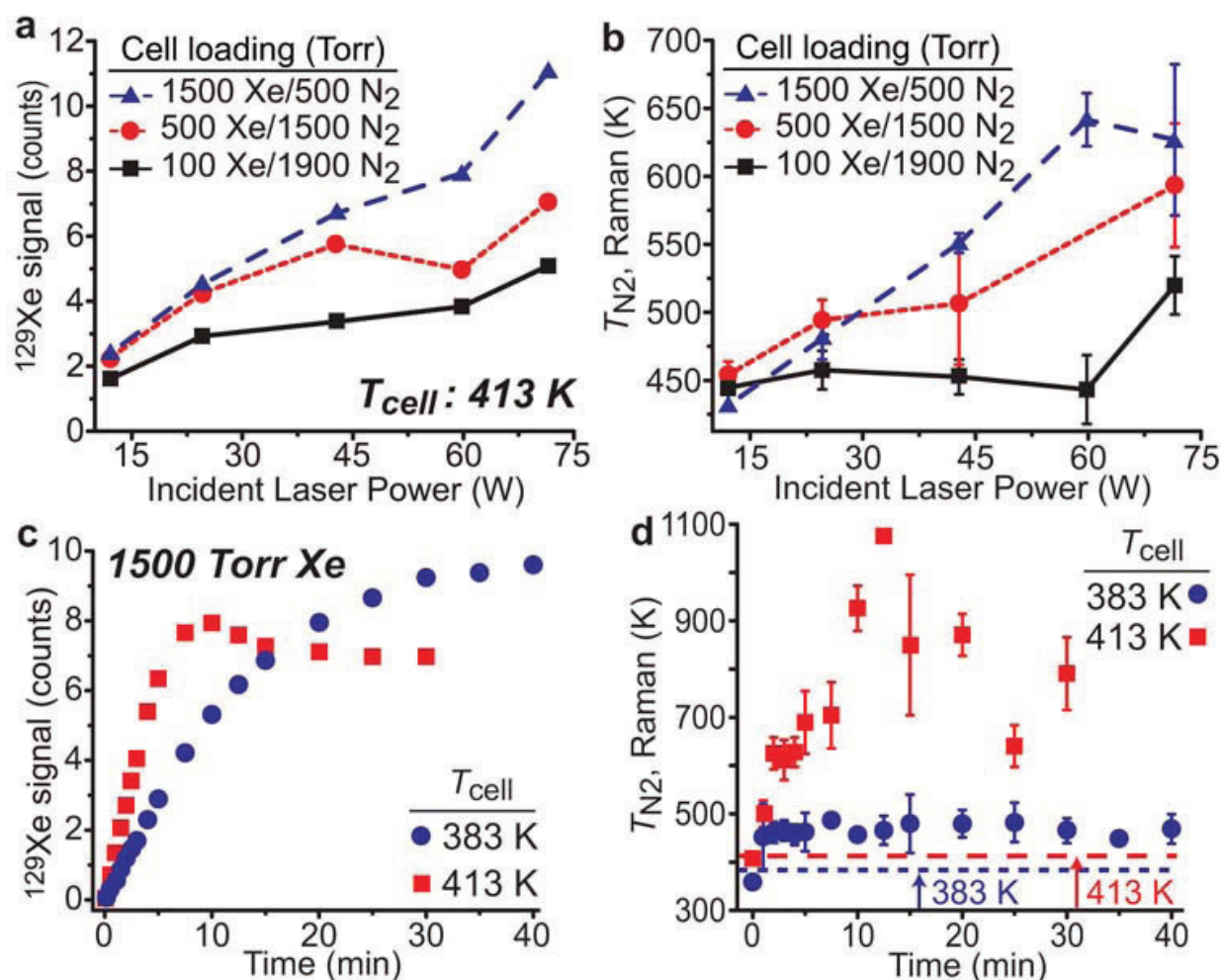

Figure 5. (a) Plot of ^{129}Xe NMR signal versus incident laser power for three Xe/N_2 gas mixtures (values in Torr): 100/1900 (solid); 500/1500 (dotted); and 1500/500 (dashed). (b) Concurrent N_2 rotational temperatures for the experiment in (a) (y-axis baseline set to T_{cell}). (c) Time course of ^{129}Xe NMR signal recorded during SEOP performed at two different oven surface temperatures: 383 K (squares) and 413 K (circles) for a cell loading of 1500/500 Torr Xe/N_2. (d) Concurrent N_2 rotational temperatures for the experiment in (c). Upper limits of T_{cell} are shown as dotted (383 K) and dashed (413 K) lines [17].

3.2. In-line superhead

In an attempt to overcome the limitations of the orthogonal Raman probe arrangement, a confocal approach was taken whereby scattered photons were detected in the same plane as probe laser photon emission. To realize this, the same 532 nm probe laser and Horiba Jobin-Yvon U1000 double 1-m Raman spectrometer (from Section 3.1) were fiber-coupled instead to an on-axis optical module. This design greatly improved the sensitivity and reliability of the measurements due to the significantly reduced chance of misalignment relative to the orthogonal arrangement. Two ultra-narrow-band VHG notch filters were used to discard the vast majority of dominant Rayleigh scattered light, allowing resolution of both Stokes and anti-Stokes ultra-low frequency Raman lines as close as 10 cm^{-1} to the probe laser wavelength. Rayleigh scattered light was further reduced by an order of magnitude through the inclusion of an ultra-narrow-band beamsplitter filter, which also facilitated the minimization of spontaneous laser diode emissions and fluorescence, thus greatly improving the spectra of the incoming probe photons [19]. Additionally, the entire configuration is mounted on a translational x-axis stage, allowing different positions within the optical cell to be probed independently. Schematics of the inline configuration are shown in **Figure 6**, along with a typical Raman spectrum and temperature calibration plot to illustrate the improvements in sensitivity.
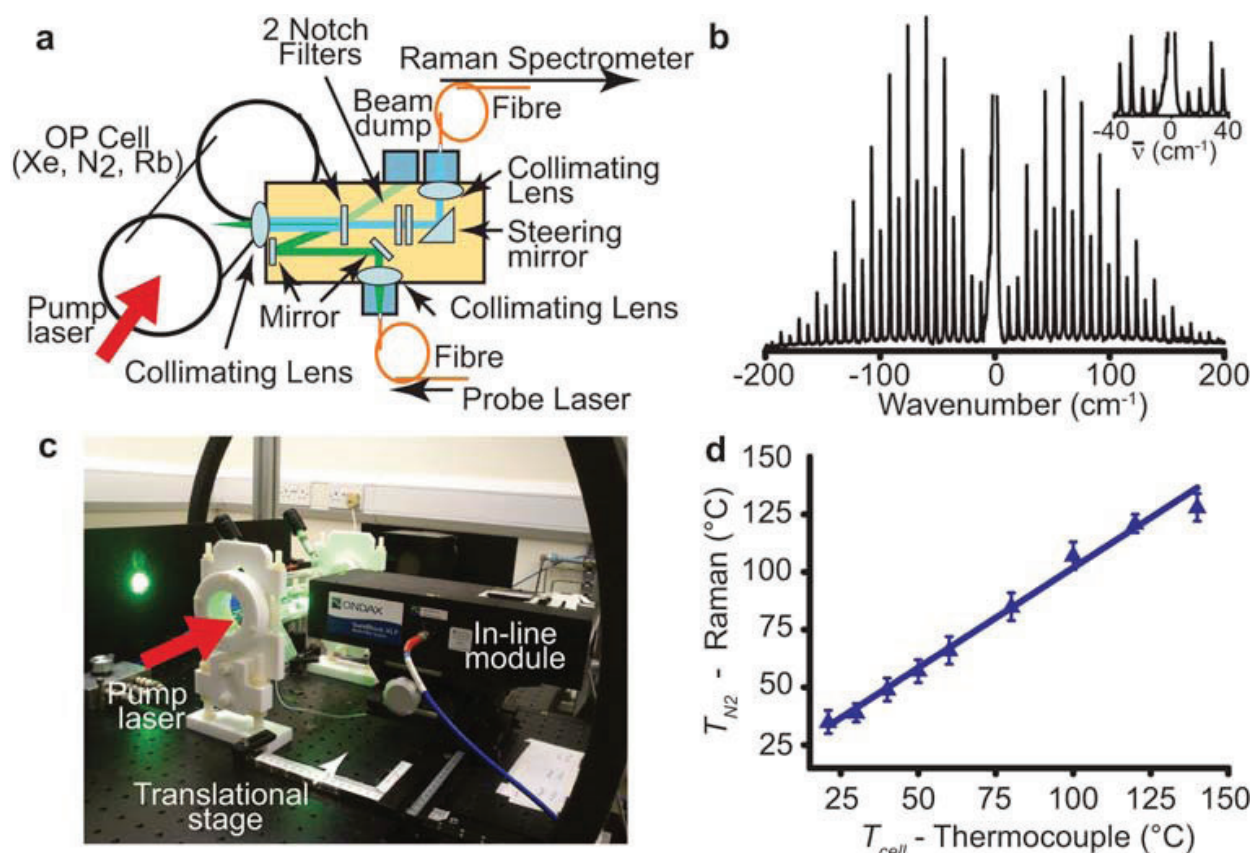

Figure 6. (a) Schematic representation of in-line Raman module. (b) Example N_2 rotational Raman spectrum (baseline-corrected) at room temperature, without SEOP (3 atm N_2). The inset shows a close-up of the ultra-low frequency region that is spectrally resolvable using the in-line apparatus. (c) Photograph of in-line Raman module. The inline module is mounted onto a translational stage to allow three-dimensional mapping of T_{N2} within the cell. (d) Plot of oven temperature (T_{cell}) measured via thermocouple (located in the oven inlet airstream) versus T_{N2} measured via Raman spectroscopy; experimental data (triangles) are shown in comparison with simulation assuming 1:1 correlation (line); error bars are least-squares fit errors of Bhc/kT plots [19].

A comparison of Raman spectra acquired using the orthogonal and in-line methods was made under identical conditions at room temperature, with no pump laser illumination and over a 15 s integration time in an optical cell containing 100/1900 Torr Xe/N_2. The results of this experiment are shown in **Figure 7**, indicating a ~23-fold improvement in SNR [19], facilitating much more accurate determination of temperature. It can be seen from the spectra that additional Raman signals arise from atmospheric N_2 and O_2 along the optical path of the probe laser external to the optical cell. In later studies, these contributions to the Raman spectrum were mitigated by collection of spectra from an evacuated optical cell, which were subsequently subtracted from the data to remove "background" signals. Care must be taken during this correction process, however, as spectral drift can result in unrealistic difference spectra and less precise temperature measurements.
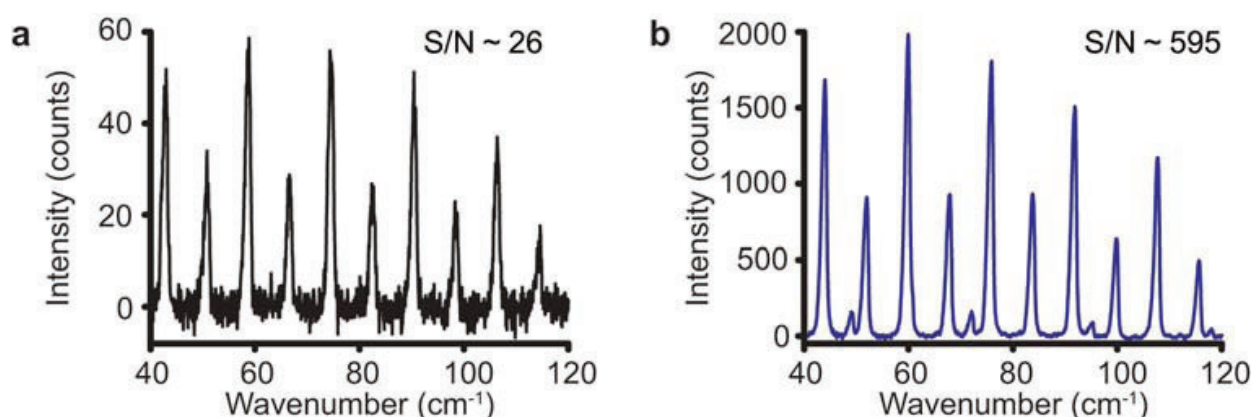

Figure 7. Comparison of typical rotational Raman spectra from N_2 gas at 24°C using the 'orthogonal' detection system (a) or the 'inline' module (b). Spectra were obtained under identical conditions (OP cell containing 100/1900 Torr Xe/N_2, 15 s acquisition time, no pump laser illumination), and indicate a SNR improvement of ~23-fold when using the in-line apparatus [19].

As an initial demonstration of temperature determination *in situ* during SEOP, the effects of cell heating due to the pump laser were investigated by comparing the T_{N2} spatial profile along the *z*-axis after 5 min of pump laser illumination at 60 W, for both a frequency-narrowed and broadband laser diode array. The gas mixture was an identical 100/1900 Torr Xe/N_2 mixture, while the temperature at the inlet to the external forced air oven was 150°C. Measurements were taken across the optical cell at intervals of 1 mm transverse to the pump laser beam, at an *x*-position 21 mm behind the front window. The resulting Raman spectra were analyzed to calculate T_{N2} across the width of the cell. It was observed that for both pump laser sources, temperatures were elevated relative to thermocouple readings in the external forced air oven; by roughly 40°C in the case of broadband pump laser illumination, but by as much as 200°C when using the frequency-narrowed pump laser. This can be explained by a greater proportion of photons from the frequency-narrowed pump laser possessing the energy required to induce an energy level transition within the alkali metal electrons. The higher number of polarized electrons directly leads to an increase in the amount of energy imparted to the rovibrational states of N_2 as a result of quenching collisions. The results of this experiment are shown in **Figure 8** along with spectral profiles of the two different lasers used.
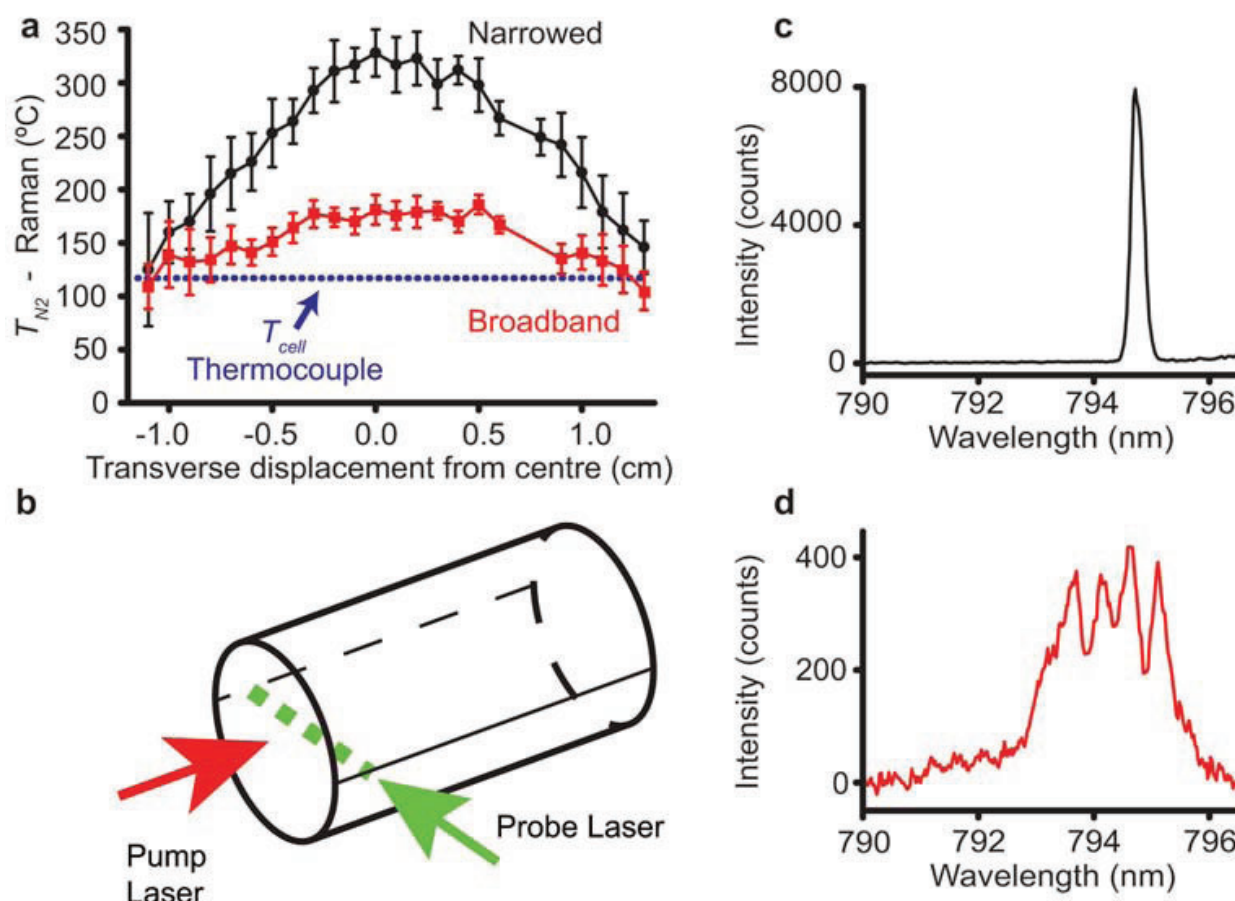
Figure 8. (a) Plots showing the spatial variation of the steady-state values of T_{N2} during SEOP, as induced by the 'pump' LDAs [acquired after 5 min of illumination by either a 60 W broadband (red squares) or 60 W VHG-narrowed LDA (black circles)]. Plots are compared to the temperature of the external glass wall near the front of the cell, as measured with a thermocouple (dotted line). (b) Schematic representation detailing the collection of T_{N2} data; values for T_{N2} were measured in 1-mm increments by translating the focused spot horizontally across the cross-section of the cell, transverse to the pump beam. (c, d) Spectral profiles of the VHG-narrowed and broadband LDAs, respectively; FWHM = 0.26 and 2.13 nm [19].

4. Current work and future directions

Since demonstrating its utility and improved performance, the in-line Raman module has become central to our current work: a series of experiments that provide greater insight into xenon-rich stopped-flow SEOP. So far, these experiments have examined SEOP as a function of (1) buffer gas, in which the ratio of N_2 to He was varied; (2) position within the optical cell, in which the portable nature of the in-line Raman module was harnessed to probe in-cell temperatures at multiple points along the length of the optical cell; and (3) alkali metal ratio (the so-called hybrid SEOP), in which pure Rb SEOP was compared to SEOP with Cs also present in the optical cell in varying amounts. The rationale, results, and implications of these experiments are described in the following sections.

4.1. Function of buffer gas/mixture composition

There are two primary buffer gases that are typically utilized in SEOP experiments—N_2 and He. N_2 is used to perform radiation trapping, quenching the emission of resonant unpolarized photons by excited alkali metal atoms that would otherwise depolarize other Rb atoms. He meanwhile was originally added in high fractions to collisionally broaden the absorption line of the alkali metal to more optimally couple the incident laser line [20], a job to which it was well suited due to its low Rb spin-destruction rate—see **Table 1**. N_2 also provides pressure-broadening effects, albeit at the cost of increased spin-destruction. This practice was necessary because the pump laser linewidths were initially at least an order of magnitude wider than the Rb D_1 transition line, resulting in inefficient optical pumping. Although the role of He for pressure-broadening has become increasingly redundant as pump laser linewidths narrow to approach the Rb linewidth, its high thermal conductivity relative to N_2 and Xe is important to note. In the emerging regime of ^{129}Xe-rich stopped-flow SEOP, where both the poor thermal conductivity of the Xe and longer gas residence time in the cell compound thermal runaway issues, He may be uniquely situated to facilitate the dissipation of thermal energy from the optical cell, ultimately improving yields of polarized ^{129}Xe.

Gas	Thermal conductivity (10^{-2} W m^{-1} K^{-1})	Spin destruction rate (cm^3 s^{-1})
Xenon	0.70	6.02×10^{-15} (T/298 K)
Nitrogen	3.09	3.44×10^{-18} (T/298 K)
Helium	17.77	3.45×10^{-19} (T/298 K)

Table 1. Thermal conductivities and spin destruction rates for Xe and N_2/He buffer gases used in the SEOP hyperpolarization process [21].

The impact of He on the thermal behavior within the optical cell can be seen in **Figure 9**. Here, three SEOP experiments are compared in which the partial pressure of Xe and the total cell pressure were held constant at 100 Torr and 2000 Torr, respectively, but increasing amounts of He gas were substituted in place of N_2. As the fraction of He within the cell was increased it can be seen that T_{N2} is reduced from roughly 200°C with no He present, to 100°C with 1400 Torr He included in the mixture. The onset of Rb runaway is evident from the sharp spike in ^{129}Xe polarization in the first mix, where the polarization initially climbs sharply, peaking abruptly at ~6 min before dropping. At this point the high Rb vapor density creates optical opacity that limits the polarization process. It can be seen that this effect is suppressed as more He is added to the mixture at little cost to the ultimate ^{129}Xe polarization. Given that existing ^{129}Xe-rich stopped-flow polarizers operate with substantially higher powered lasers, which only further exacerbate these thermal management issues, it may be that He becomes a valuable tool for optimization.
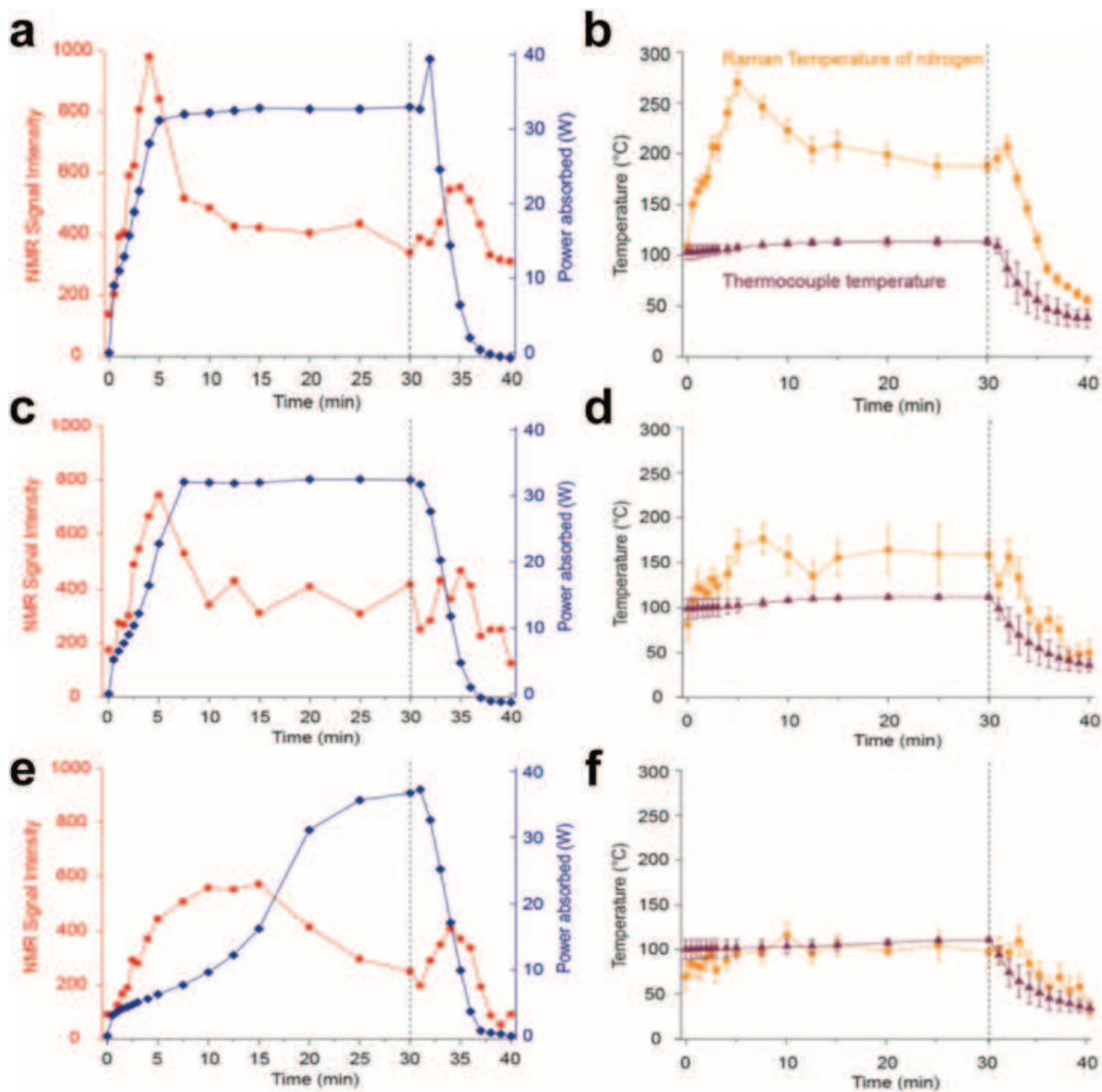
Figure 9. Comparison of SEOP as a function of buffer gas composition—(a), (c), and (e) show Xe polarization (red) and power absorbed (blue). (b), (d), and (f) show N_2 Raman temperature (orange) and oven thermocouple temperature (green). Gas compositions were 100/1900 Torr Xe/N_2 with no He (a, b), 100/1700 Torr Xe/N_2 and 200 Torr He (c, d), and 100/500 Torr Xe/N_2 and 1400 Torr He (e, f) [22].

4.2. Position-dependent temperature mapping

The experiments that vary buffer gas density/composition indicate that polarization and temperature are likely to vary along the length of the cell, particularly under conditions of Rb runaway. **Figure 10** illustrates how Raman measurements were taken at coincident locations to NMR measurements at the front, middle, and back of the optical cell (a) using the translational stage (b). **Figure 11** shows the results of two experiments where this configuration was used. Both experiments were conducted on a gas mix of 1000/1000 Torr Xe/N_2 but at oven temperatures of 120 and 130°C, respectively. At 120°C, the temperature at the front, middle, and back correspond well to the xenon polarizations, which are both highest at the back for the cell.

However, it can be seen that a mere 10°C increase in oven temperature is enough to induce significant variation in T_{N2} along the length of the cell. Closer examination shows that after 4 min of pump laser illumination during SEOP, when the [129]Xe polarization prematurely spikes, a switch in the Raman temperatures occurs–indicative of a change in the thermal flow patterns within the cell. This effect is likely caused by Rb runaway, a conclusion corroborated by the elevated pump laser light absorption, which indicates a spike in absorbers.
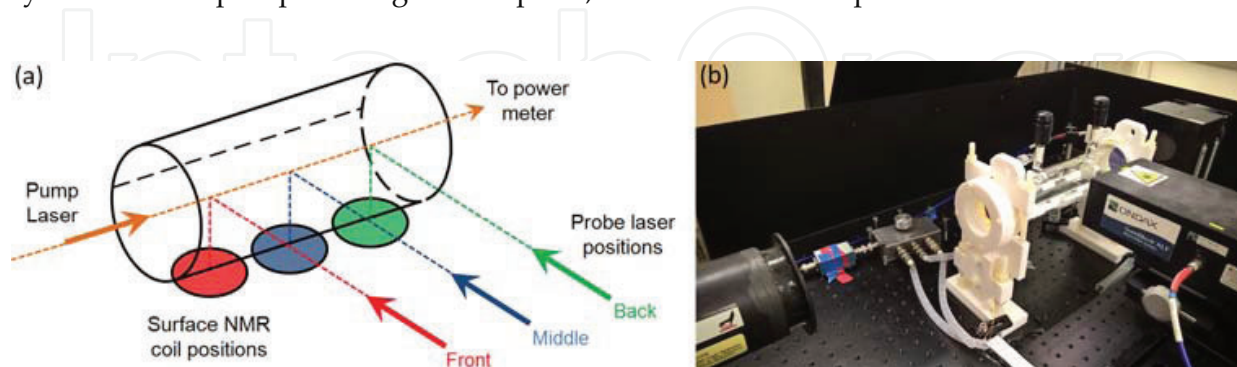

Figure 10. (a) Schematic representation showing in-line Raman module probe and NMR surface coil alignment at three positions within the optical pumping cell. (b) Photograph of in-line Raman module and NMR surface coils placed within the oven [23].
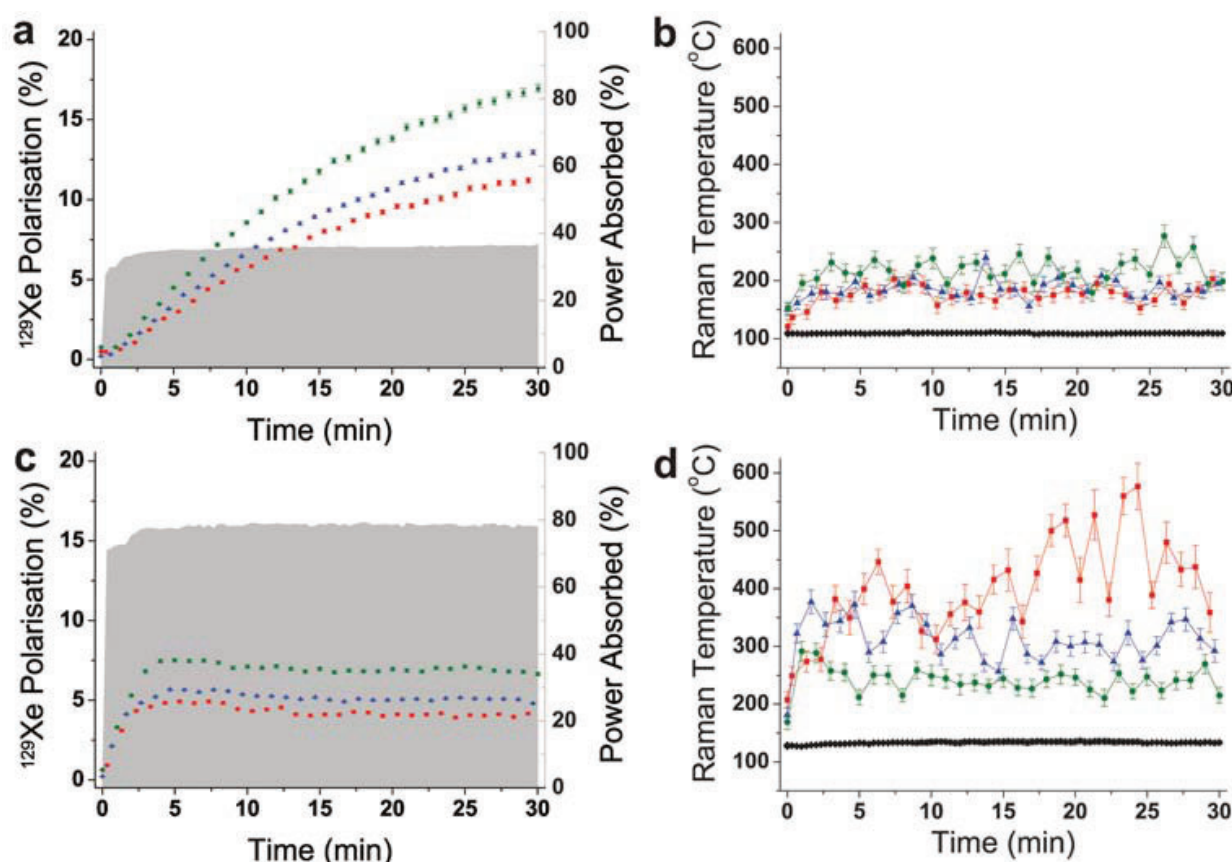

Figure 11. Comparison of Xe polarization build-up and T_{N2} Raman measurements during a 30-min SEOP experiment in an optical pumping cell containing 1000/1000 Torr Xe/N_2 at 120°C (a, b) and 130°C (c, d). Line color is indicative of cell position as outlined in **Figure 10(a)**. The shaded area in figures (a) and (c) represents the percentage of pump laser light absorbed [23].

These measurements as a function of position will be improved by introducing an auto-
mated translational stage that will permit more reliable positioning of the Raman probe
relative to the cell with increased speed and precision. This will facilitate N_2 temperature
maps in two dimensions—both along the width and the length of the optical cell.
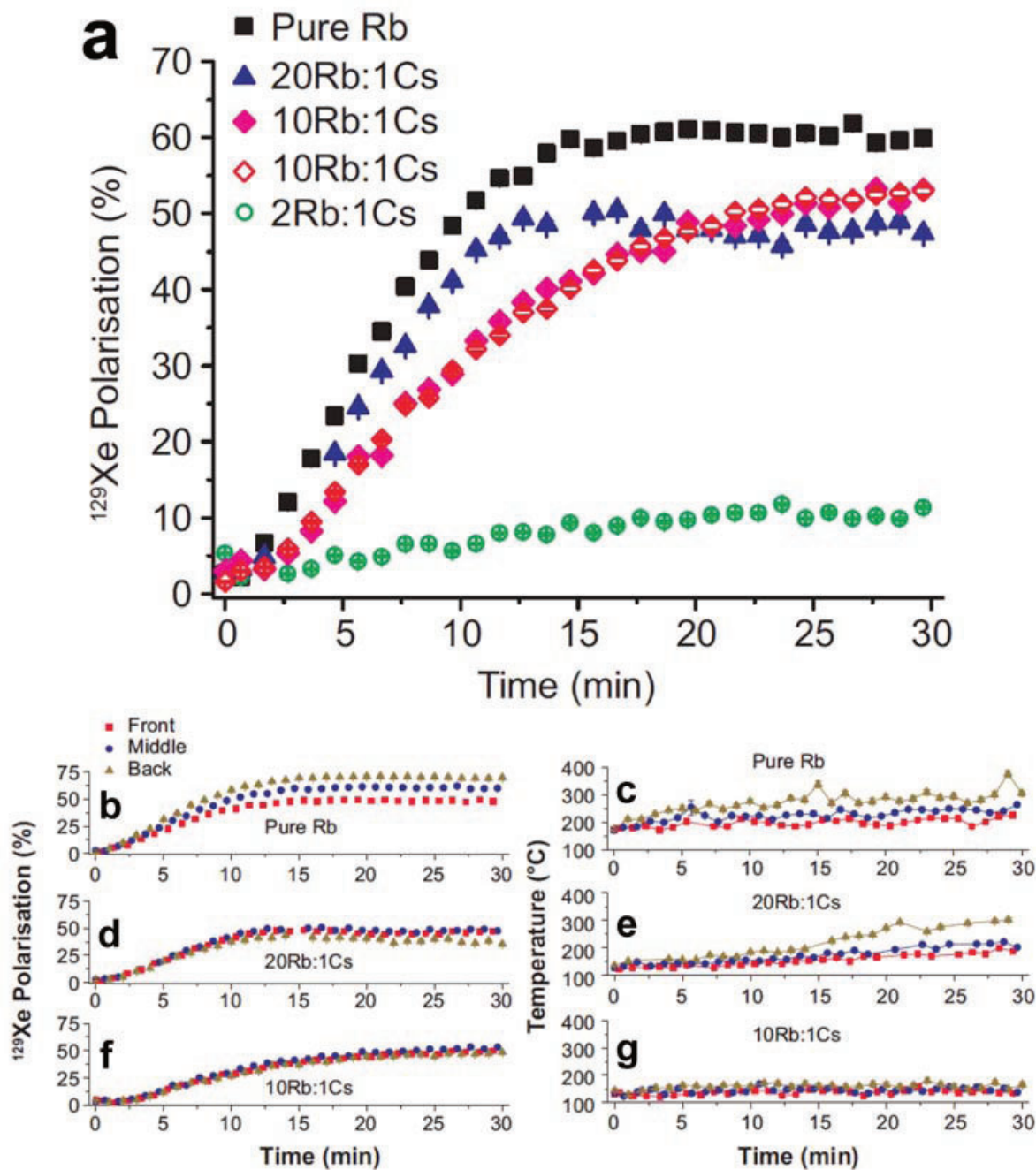

Figure 12. Rb-Cs hybrid SEOP. (a) [129]Xe polarization build-up curves using pure Rb, 20Rb:1Cs, 10Rb:1Cs, 2Rb:1Cs. Solid
colored symbols denote a premixing of the AMs before loading; empty symbols denote separate loading. (b), (d), and (f)
show xenon polarizations for the front middle and back positions within the cell for pure Rb, 20Rb:1Cs, 10Rb:1Cs and (c),
(e), and (g) show the corresponding Raman temperatures. Cell oven temperature was set to 140°C and the gas mixture
was 100/1900 Torr Xe/N_2 [24].

4.3. Function of alkali metal ratio (Rb-Cs hybrid SEOP)

Rubidium has long been the alkali metal of choice for SEOP, owing to its large absorption cross-section and the availability of affordable, high-powered lasers that are well matched to its D_1 transition line. Additionally, Rb is solid at room temperature, with a low melting point that facilitates easy storage and transfer into optical cells. However, it has been shown that cesium can produce greater polarization under similar experimental conditions [25], but comparably high-powered lasers at the Cs D_1 transition wavelength are not commonplace. Alternatively, for ^{3}He hyperpolarization by SEOP, it was shown that using two alkali metals simultaneously—rubidium and potassium—resulted in four times faster build-up of net spin polarization once the optimal ratio of the alkali metals had been achieved [26]. In this example it was Rb that underwent optical pumping, with angular momentum transferred to He by two distinct spin-exchange routes; one directly from Rb to He, and from Rb to He via K. The reason for the increase in speed is that the exchange cross sections for Rb-K and K-He are both larger than those for Rb-He alone. Inspired by these findings, we conducted analogous experiments in an Rb-Cs SEOP system to hyperpolarize ^{129}Xe. The SE cross-sections for Rb-Cs and Cs-Xe have been shown to be greater than for Rb-Xe in separate experiments [27, 28]. If successful, the performance of existing polarizers could be improved with the simple addition of Cs to the existing Rb within the optical cell. As with previous studies, a 60 W pump laser tuned to the Rb D_1 transition wavelength was used for polarization.

Figure 12(a) shows a summary of major hybrid results to date. From this figure it can be seen that, contrary to that suggested by the SE cross-sections, the resulting ^{129}Xe polarization in our initial efforts decreases as more Cs is added to the alkali metal hybrid mixture. The data in **Figure 12(b–g)** can be used to explain this observation, indicating that ^{129}Xe polarization and T_{N2} actually decrease with increasing Cs fraction. The latter is indicative of decreasing rates of optical pumping, likely caused by a suppression of the Rb vapor by a dominant Cs vapor. Indeed, the intrinsic vapor pressure of Cs is higher than that of rubidium due to its lower boiling point, a relation that is reversed in the analogous K-Rb system for ^{3}He hyperpolarization. Thus, our Rb-Cs hybrid experiments to date indicate that the addition of Cs to the standard Rb-^{129}Xe SEOP method serves only to suppress the ^{129}Xe polarization. However, considering only a small number of different Rb-Cs ratios and conditions have been investigated, future studies on leaner Cs mixtures, where the Rb vapor density is not suppressed to such an extent, may yet yield a more favorable outcome.

5. Conclusions

An overview of gas temperature measurement using Raman spectroscopy and its potential as a diagnostic tool for improving understanding of energy transport processes during spin-exchange optical pumping has been discussed. The main approaches taken to correlate low-field NMR with Raman spectroscopy, using both orthogonal and in-line detection methods, have been compared and contrasted to relevant historical studies as well as each other to provide insight on poorly understood thermal processes present during SEOP. Future research will aim to build upon the in-line configuration, where automation of the translational stage

could allow three-dimensional temperature mapping for improved characterization of these processes with greater resolution. Additionally, the demand for higher laser powers and richer Xe mixtures will likely result in thermal management becoming paramount, as the tightrope between maximizing polarization efficiency and avoiding the perilous "runaway" regime becomes narrower still.

This improved understanding of such thermal and energy transport processes should be directly translated to improving the next generation of clinical hyperpolarizers for use in producing HP noble gas for MRI studies in the lungs, which will hopefully facilitate safer, earlier, and more reliable diagnosis of a variety of serious and life-threatening diseases. Such advances will serve to streamline the diagnostic process, improving cost-effectiveness and reducing strain on medical services alongside the obvious benefit to those in society.

Author details

Jonathan Birchall[1]*, Nicholas Whiting[2], Jason Skinner[1], Michael J. Barlow[1] and Boyd M. Goodson[3]

*Address all correspondence to: msxjrb@nottingham.ac.uk

1 Sir Peter Mansfield Imaging Centre, University of Nottingham, Nottingham, UK

2 The University of Texas MD Anderson Cancer Center, Houston, TX, USA

3 Department of Chemistry and Biochemistry, Southern Illinois University, Carbondale, IL, USA

References

[1] Erkonen WE, Smith WL, editors. Radiology 101: The Basics and Fundamentals of Imaging. 3rd ed. Philadelphia: Lippincott, Williams and Wilkins; 2010. 8 p. DOI: http://dx.doi.org/10.1016/j.acra.2010.01.022.

[2] Walker TG, Happer W, Spin-exchange optical pumping of noble-gas nuclei. Reviews of Modern Physics. 1997;69:629. DOI: http://dx.doi.org/10.1103/RevModPhys.69.629.

[3] Appelt S, Ünlü T, Zilles K, Shah NJ. Experimental studies of rubidium absolute polarization at high temperatures. Applied Physics Letters. 1999;75:428. DOI: 10.1063/S0003-6951 (99)03229-5.

[4] Walter DK, Griffith WM, Happer W. Energy transport in high-density spin-exchange optical pumping cells. Physical Review Letters. 2001;86:3264-3267. DOI: http://dx.doi.org/10.1103/PhysRevLett.86.3264.

[5] Zook AL, Adhyaru BB, Bowers CR. High capacity production of > 65% spin polarized xenon-129 for NMR spectroscopy and imaging. Journal of Magnetic Resonance. 2002;159:175-182. DOI: 10.1016/S1090-7807(02)00030-7.

[6] Whiting N, Nikolaou P, Eschmann NA, Goodson NM, Barlow MJ. Interdependence of in-cell xenon density and temperature during $Rb/^{129}Xe$ spin-exchange optical pumping using VHG-narrowed laser diode arrays. Journal of Magnetic Resonance. 2011;208:298-304. DOI: 10.1016/j.jmr.2010.11.016.

[7] Goodson BM, Nuclear magnetic resonance of laser-polarized noble gases in molecules, materials, and organisms. Journal of Magnetic Resonance. 2002;155:157-216. DOI: 10.1006/jmre.2001.2341.

[8] Romalis MV, Miron E, Cates GD. Pressure broadening of Rb D_1 and D_2 lines by ^3He, ^4He, N_2, and Xe: Line cores and near wings. Physical Review A. 1997;56:4569-4578. DOI: http://dx.doi.org/10.1103/PhysRevA.56.4569

[9] Breeze SR, Lang S, Moudrakovski I, Ratcliffe CI, Ripmeester JA, Santyr G et al. Coatings for optical pumping cells and short-term storage of hyperpolarized xenon. Journal of Applied Physics. 2000;87:8013-8017. DOI: http://dx.doi.org/10.1063/1.373489.

[10] Fink A, Baumer D, Brunner E. Production of hyperpolarized xenon in a static pump cell: Numerical simulations and experiments. Physical Review A. 2005;72:053411. DOI: http://dx.doi.org/10.1103/PhysRevA.72.053411.

[11] Fink A, Brunner E. Optimization of continuous flow pump cells used for the production of hyperpolarized ^{129}Xe: A theoretical study. Applied Physics B. 2007;89:65-71. DOI: 10.1007/s00340-007-2754-z.

[12] Hickman RS, Liang LH. Rotational temperature measurement in nitrogen using Raman spectroscopy. Review of Scientific Instruments. 1972;43:796–799. DOI: http://dx.doi.org/10.1063/1.1685760.

[13] Nikolaou P, Coffey AM, Walkup LL, Gust BM, Whiting N, Newton H, et al. Near-unity nuclear polarization with an 'Open-Source' ^{129}Xe hyperpolarizer for NMR and MRI. Proceedings of the National Academy of Sciences 2013;110:14150–14155. DOI: www.pnas.org/cgi/doi/10.1073/pnas.1306586110.

[14] Dregely I, Mugler JP 3rd, Ruset IC, Altes TA, Mata JF, Miller GW, et al. Hyperpolarized xenon-129 gas-exchange imaging of lung microstructure: first case studies in subjects with obstructive lung disease. Journal of Magnetic Resonance Imaging 2011;33:1052–1062. DOI: http://dx.doi.org/10.1002%2Fjmri.22533.

[15] Safavi S, Barlow M, Hall I. Clinical ^{129}Xe aspects of translation of HP Xenon-129. Manuscript in preparation.

[16] Whiting N, Nikolaou P, Eschmann NA, Barlow MJ, Lammert R, Ungar J, et al. Using frequency-narrowed, tunable laser diode arrays with integrated volume holographic gratings for spin-exchange optical pumping at high resonant fluxes and xenon densities. Applied Physics B 2012;106:775–788. DOI: 10.1007/s00340-01204924-x.

[17] Whiting N. Manuscript in preparation.

[18] Rosen MS, Chupp TE, Coulter KP, Welsh RC. Polarized [129]Xe optical pumping/spin exchange and delivery system for magnetic resonance spectroscopy and imaging studies. Review of Scientific Instruments. 1999;70:1546-1552. DOI: 10.1063/1.1149622.

[19] Newton H, Walkup LL, Whiting N, West L, Carriere J, Havermeyer F, et al. Comparative study of in situ N2 rotational Raman spectroscopy methods for probing energy thermalisation processes during spin-exchange optical pumping. Applied Physics B 2014;115:167–172. DOI: 10.1007/s00340-013-5588-x.

[20] Driehuys B, Cates GD, Miron E, Sauer K, Walter DK, Happer W. High-volume production of laser-polarized [129]Xe. Applied Physics Letters. 1996;69:1668-1670. DOI: 10.1063/1.117022

[21] Tables of Physical & Chemical Constants (16th edition 1995). 2.3.7 Thermal conductivities [homepage on the Internet]. Kaye & Laby Online. [updated c2005; cited 2016 Sep 26]. Available from: http://www.kayelaby.npl.co.uk/general_physics/2_3/2_3_7.html

[22] Newton H, Smith J, Walkup L, Whiting N, Barlow M, Morris P et al. Effects of gas composition on optical pumping and energy transport for hyperpolarized 129Xe using in situ Raman spectroscopy and NMR. Poster session presented at: Exotica, 54th Experimental Nuclear Magnetic Resonance Conference; 2013 Apr 14-19; Pacific Grove, CA.

[23] Birchall J. Manuscript in preparation.

[24] Newton H, Skinner J, Birchall J, Whiting N, Gust BM, Ranta K et al. Can We Utilise Rb/Cs Hybrid optical pumping to hyperpolarise noble gases? Presentation given at: Sensitivity and Resolution: Pushing the Boundaries, 55th Experimental Nuclear Magnetic Resonance Conference; 2014 Mar 23-28; Boston, MA.

[25] Whiting N, Eschmann NA, Goodson BM. [129]Xe-Cs (D_1, D_2) versus [129]Xe-Rb (D_1) spin-exchange optical pumping at high xenon densities using high-power laser diode arrays. Physical Review A 2011;83:053428. DOI: http://dx.doi.org/10.1103/PhysRevA.83.053428.

[26] Babcock E, Nelson I, Kadlecek S, Driehuys B, Anderson LW, Hersman FW, et al. Hybrid spin-exchange optical pumping of [3]He. Physical Review Letters. 2003;91:123003. DOI: http://dx.doi.org/10.1103/PhysRevLett.91.123003.

[27] Gibbs H, Hull R. Spin-exchange cross sections for Rb[87]-Rb[87] and Rb[87]-Cs[133] collisions. Physical Review. 1967;153:132. DOI: http://dx.doi.org/10.1103/PhysRev.153.132.

[28] Jau Y-Y, Kuzma NN, Happer W. High-field measurement of the [129]Xe – Rb spin-exchange rate due to binary collisions. Physical Review A 2002;66:052710. DOI: http://dx.doi.org/10.1103/PhysRevA.66.052710.